ACS APPLIED MATERIALS & INTERFACES

www.acsami.org

Forum Article

Single Nanoflake Photoelectrochemistry Reveals Intrananoflake Doping Heterogeneity That Explains Ensemble-Level Photoelectrochemical Behavior

Michael Van Erdewyk and Justin B. Sambur*

Cite This: https://doi.org/10.1021/acsami.1c14928

Read Online

ACCESS | Metrics & More | Article Recommendations | Supporting Information

ABSTRACT: Transition metal dichalcogenide (TMD) nanoflake thin films are attractive electrode materials for photoelectrochemical (PEC) solar energy conversion and sensing applications, but their photocurrent quantum yields are generally lower than those of bulk TMD electrodes. The poor PEC performance has been primarily attributed to enhanced charge carrier recombination at exposed defect and edge sites introduced by the exfoliation process. Here, a single nanoflake PEC approach reveals how an alternative effect, doping heterogeneity, limits ensemble-level PEC performance. Photocurrent mapping and local photocurrent–potential (i–E) measurements of MoS_2 nanoflakes exfoliated from naturally occurring bulk crystals revealed the presence of n- and p-type domains within the same nanoflake. Interestingly, the n- and p-type domains in the natural MoS_2 nanoflakes were equally efficient for iodide oxidation and tri-iodide reduction (IQE values exceed 80%). At the single domain-level, the natural MoS_2 nanoflakes were nearly as efficient as nanoflakes exfoliated from synthetic n-type MoS_2 crystals. Single domain-level i–E measurements explain why natural MoS_2 nanoflakes exhibit an n-type to p-type photocurrent switching effect in ensemble-level measurements: the n- and p-type diode currents from individual domains oppose each other upon illuminating the entire nanoflake, resulting in zero photocurrent at the switching potential. The doping heterogeneity effect is likely due to nonideal stoichiometry, where p-type domains are S-rich according to XPS measurements. Although this doping heterogeneity effect limits photoanode or photocathode performance, these findings open the possibility to synthesize efficient TMD nanoflake photocatalysts with well-defined lateral p- and n-type domains for enhanced charge separation.

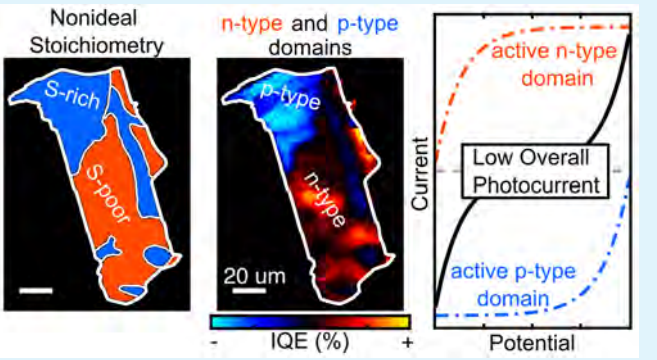

KEYWORDS: *2D materials, single nanoflake, photocurrent mapping, n-type MoS_2, p-type MoS_2*

INTRODUCTION

Transition metal dichalcogenides (TMDs) such as WSe_2 and MoS_2 are promising light harvesting materials for photoelectrochemical (PEC) solar energy conversion applications because they exhibit long-term stability[1] and nearly optimum band gaps for solar photon capture.[2−5] One advantage of their layered crystal structure is bulk TMDs can be exfoliated into two-dimensional (2D) nanoflakes and then processed into large-area thin film photoelectrodes.[6−8] For example, Wells et al. demonstrated a high-throughput roll-to-roll deposition process that first exfoliates MoS_2 nanoflakes from commercially available powders using solvents and then deposits 10 cm wide films on electrode surfaces.[9] Advances in mechanical exfoliation have also led to the production of high-quality macroscopic monolayers and artificial heterostructures,[10,11] which opens the exciting possibility of creating macroscopic p–n junctions with controllable properties defined by the parent bulk material. Hence, the 2D materials community is advancing large-scale production methods for potentially low-cost and high-performance thin film photoelectrodes.[12−14]

Unfortunately, TMD nanoflake thin films have not achieved the same photoelectrochemical performance as bulk TMDs. In the 1980s, several groups demonstrated efficient bulk TMD|I^-,I_2|Pt PEC solar cells.[1,3,15,16] The PEC solar cells achieved >70% internal quantum efficiency (IQE) at zero applied bias and maintained >10% power conversion efficiency for more than one month of continuous operation.[1,5] On the other hand, TMD nanoflake photoelectrodes produce much lower photocurrent densities for the same iodide oxidation reaction even under applied bias. For example, uniform 0.26 cm^2 MoS_2/WSe_2 nanoflake electrodes produced 40 $\mu A\ cm^{-2}$ under 100 mW/cm^2 illumination,[9] whereas 0.05 cm^2 bulk MoS_2, WS_2,

Special Issue: Early Career Forum

Received: August 5, 2021
Accepted: October 15, 2021

and WSe_2 electrodes produced 6−10 mA/cm^2 under 80−90 mW/cm^2 illumination.[17] TMD nanoflakes can exhibit high (60−80%) internal quantum efficiency (IQE) values for the iodide oxidation reaction under applied bias,[18] but the fill factor of nanoflake electrodes is about a factor of 2 worse than that of bulk TMD photoelectrodes.[1,5,19] Bulk TMDs[20] also out-perform nanoflakes in the PEC hydrogen evolution reaction.[21,22] Light absorption differences between bulk and nanoflake photoelectrodes cannot fully account for the significant performance gap.[6]

One likely contribution to the poor performance of nanoflake photoelectrodes is the high number of exposed defect and edge sites after the exfoliation process.[18,22] Exposed edge sites of TMD photoanodes were identified as potent recombination centers decades ago.[4,5,23−30] Specific chemical treatments have been developed to mitigate charge carrier recombination at edge sites on both bulk and nanoflake electrodes.[5,22,31−33]

Considerably less attention has been paid to PEC performance variation among apparently smooth basal planes within single nanoflakes. Velický et al. discovered that layer thickness and light intensity influenced the PEC performance of basal planes within mono- and few-layer MoS_2 nanoflakes.[34] Todt et al. attributed the heterogeneous activity of different basal planes to surface defects and impurities.[18] Additional single nanoflake-level PEC and electrocatalytic measurements reported performance variations among different basal planes on the same nanoflake.[35−38] However, the materials chemistry origin of PEC performance variation among nanoflake basal planes has not been elucidated.

One possible explanation for PEC performance variation among apparently smooth basal planes is doping heterogeneity. Hill and co-workers observed anodic to cathodic photocurrent switching behavior for different basal planes of single nanoflakes,[35,39] suggesting doping heterogeneity exists within the flake. In the early 1980s, Menezes and Lewerenz reported doping heterogeneity limits the photoelectrochemical efficiency of synthetic bulk TMD crystals.[40,41] Similarly, Kline and Parkinson provided some evidence that bulk MoS_2 and WSe_2 photoelectrodes with ideal stoichiometry exhibited better photovoltage, open-circuit potential, and fill factor than crystals with nonideal stoichiometry.[17] Spatially resolved PEC measurements of bulk TMD crystals revealed similar results.[29,42,43] Lewis and co-workers reported the external quantum yield of different basal planes on p-WSe_2 varied due to differences in local electronic structure.[29] MoS_2 nanoflakes exfoliated from naturally occurring crystals exhibit ambipolar transport properties in field effect transistors.[44,45] Hence, there is significant literature precedent that doping heterogeneity in bulk TMD materials can transfer to individual nanoflakes and limit PEC performance.

In this study, we test the literature-based hypothesis that doping heterogeneity limits PEC performance of exfoliated nanoflake photoelectrodes. To test this hypothesis, we compared the PEC performance of MoS_2 nanoflakes that were mechanically exfoliated from two widely used commercial sources: synthetic n-type Re-doped MoS_2 from 2Dsemiconductors (https://www.2dsemiconductors.com/n-type-mos2/) and naturally occurring MoS_2 from SPI (https://www.2spi.com/item/z429ml/). We hypothesized that doping heterogeneity is less likely in the synthetic crystal than the naturally occurring crystal. All 21 Re-doped MoS_2 nanoflakes were efficient n-type photoanodes for iodide oxidation (IQE values exceeded 80%), confirming the ensemble-level result that the Re-doped MoS_2 nanoflake thin film produced larger photocurrents than the natural MoS_2 nanoflake film. On the other hand, photocurrent mapping and local photocurrent−potential (i−E) measurements of natural MoS_2 nanoflakes revealed the presence of n- and p-type domains within the same nanoflake. Interestingly, the n- and p-type domains were efficient for iodide oxidation and tri-iodide reduction, respectively (IQE values within single flakes exceed 80%). The single nanoflake-level i−E measurements explain the poor ensemble-level photocurrent from the natural MoS_2 nanoflake sample: the n- and p-type diode currents from individual domains oppose each other upon illuminating the entire nanoflake, resulting in a negligible total photocurrent. Although this doping heterogeneity effect limits photoanode or photocathode performance, these findings open the possibility to synthesize TMD nanoflakes with lateral p- and n-type domains for enhanced charge separation efficiency. This approach could be beneficial for photocatalytic applications.

EXPERIMENTAL METHODS

Electrode Preparation and Ensemble-Level Electrochemical Measurements. MoS_2 nanoflake-coated ITO electrodes were prepared by mechanical exfoliation of commercially available bulk MoS_2 crystals: Re-doped n-type MoS_2 (2D semiconductors, BLK-MoS2-N, doping density 10^{17}−10^{18} cm^{-3}) and naturally occurring bulk MoS_2 (SPI, 470MOS2L-AB). In a typical mechanical exfoliation procedure, low residue Nitto tape (BT-150E-CM, Nitto) was manually pressed onto the surface of bulk crystals for 10 min and then gently removed. Gentle, manual pressure was applied to the crystal surface to remove air bubbles. A commercially available gel-film (Gelfilm from Gelpak)[46] was used to transfer exfoliated MoS_2 from the Nitto tape to a precleaned ITO electrode (4−10 Ω, 25 × 75 × 1.1 mm, Delta Technologies). The ITO cleaning procedure is provided in our previous study.[18] The nanoflake-coated ITO electrodes were assembled into a three-electrode electrochemical flow cell as described previously.[18] A Pt wire served as the counter electrode and a Ag/AgI wire was used as the reference electrode. All ensemble-level photoelectrochemical measurements of MoS_2 nanoflake-coated ITO electrodes were performed in 1 M NaI/1 mM I_2 electrolytes. Electrochemical measurements with a polished 7 mm^2 glassy carbon (GC) disc electrode (CHI Instruments, CHI104) were performed in 3 mM NaI electrolyte. An Ivium potentiostat (CompactStat.h) measured current−voltage curves in a three-electrode configuration. An 8 mW 530 nm LED (ThorLabs, M530L3) illuminated the nanoflake films for ensemble-level measurements.

Scanning Photoelectrochemical Microscopy. The electrochemical flow cells were mounted on an Olympus IX73 inverted microscope equipped with confocal Raman and photoelectrochemical mapping capabilities.[18,19] In this study, 0.30−0.7 μW 415 nm laser light (Oxxius, LBX-415−120-CSB-PPA) was directed through the back port of the microscope, reflected by a 414 nm dichroic mirror (Edmund Optics, 86330) in the filter cube, and aligned on the back aperture of a 60× objective (UPLANSAPO60x/W), yielding a 0.86 μm diameter laser spot (as determined by a knife-edge scan in Figure S1) and a laser power density of 52−121 W/cm^2. All photoelectrochemical mapping experiments were performed at fixed 0.600 V vs Ag/AgI, whereas 1 M NaI/1 mM I_2 electrolyte was flowed through the cell at a rate of 25 μL/min. The total current from the electrochemical cell was measured by an Ivium CompactStat potentiostat. The analog current output from the potentiostat was measured by a Measurement Computing Data Acquisition (DAQ) card (USB-1608FS-Plus) at a rate of 25 Hz. At the same time, the DAQ card measured the XY stage position (Marzhauzer SCANplus IM). The typical step size for mapping experiments was 1 μm. The step size was adjusted to 2 μm for large area nanoflakes (e.g., >6000

https://doi.org/10.1021/acsami.1c14928
ACS Appl. Mater. Interfaces XXXX, XXX, XXX−XXX

μm^2). The photocurrent value at each stage position (i.e., pixel) represents the averaging current during a 400 ms time period, corresponding to 10 data points. The average current from the ITO background pixels was subtracted from the current at each illumination nanoflake location. We correlate the photocurrent and structural images of nanoflakes using our correlated laser reflection-photocurrent mapping procedure (details may be found in the Supporting Information of ref 47). Supporting Information Note 1 of this work describes the detailed image analysis procedures to calculate IQE values from the EQE maps.

Local Photocurrent–Potential Measurements. A focused 415 nm laser spot excited 2.3 μm^2 areas of single nanoflakes to measure local i–E curves. A lock-in detection scheme was used to sensitively measure the photoinduced current from single nanoflakes. In a typical local photocurrent–voltage curve measurement, the excitation laser was chopped at 37 Hz to induce a modulating photocurrent due to iodide oxidation or tri-iodide reduction. The chopper frequency (TTI-C995) and the analog current output from the potentiostat were fed into a Stanford Research Systems SR830 lock-in amplifier. The lock-in detected current was measured at a fixed applied potential and averaged over an 8 s period. The measurement was repeated in 3 mV increments. The signal from the lock-in was converted from arbitrary units to ampere units by determining the proportional constant from direct current measurements.

XPS Characterization. Re-MoS_2 and SPI-MoS_2 crystals were freshly cleaved using double-sided conductive carbon tape (Nisshin-EM). The MoS_2-coated tape samples were analyzed in a PHI PE-5800 X-ray photoelectron spectroscopy (XPS) system. High-resolution XPS spectra of the C, Mo, and S regions were acquired at multiple locations on each sample using an 800 μm^2 aperture. The spectra were analyzed with PHI *Multipak* software. The Mo 3d peaks were fit with two mixed Gaussian–Lorentzian peak shapes at a fixed peak separation of 3.13 eV. The S 2p peaks were fit with two mixed Gaussian–Lorentzian peak shapes at a fixed peak separation of 1.1 eV. The C 1s peak was used to correct each spectrum for charging effects.

Elemental Analysis. Following Sales et al., Re-MoS_2 and SPI-MoS_2 were immersed in a vial containing aqueous 3 M HNO_3 solution and the vial was placed in a water bath at 40 °C for 4 days.[48] Mo and S concentrations in each sample were determined via inductively coupled plasma-atomic emission spectroscopy (ICP-AES) analysis of the acidic solutions (PerkinElmer, Optima 7300 DV). Because solid Re-MoS_2 and SPI-MoS_2 material remained in the vial after 4 days, we normalized the concentration of dissolved elements to the dissolved Mo content to account for the undissolved solid (following ref 56).

Electron Microscopy. The morphology of exfoliated Re-MoS_2 and SPI-MoS_2 samples were analyzed using scanning electron microscopy (SEM) and energy-dispersive X-ray spectroscopy (EDS) in a JEOL 6500 FE-SEM electron microscope. SEM images and EDS spectra were acquired with 2 and 15 keV accelerating voltages, respectively.

RESULTS

Photoelectrochemical Characterization. Synthetic n-type Re-doped MoS_2 and naturally occurring MoS_2 crystals were purchased from 2Dsemiconductors and SPI Supplies, respectively. The crystals were mechanically exfoliated using low residue Nitto Tape and transferred to ITO electrodes with a commercially available gel-film.[46] We refer to these nanoflake-coated ITO electrodes as Re-MoS_2 and SPI-MoS_2. Figure 1a, b shows representative optical transmission images of the Re-MoS_2 and SPI-MoS_2 samples as well as the parent bulk crystals (additional images provided in Figure S2). Mechanical exfoliation produces a heterogeneous distribution of nanoflakes ranging from 25 to 210 μm in diameter and 15–70 nm in thickness. Supporting Information Note 2 describes the procedure for thickness determination. The heterogeneous nanoflake population motivates our single nanoflake-level PEC

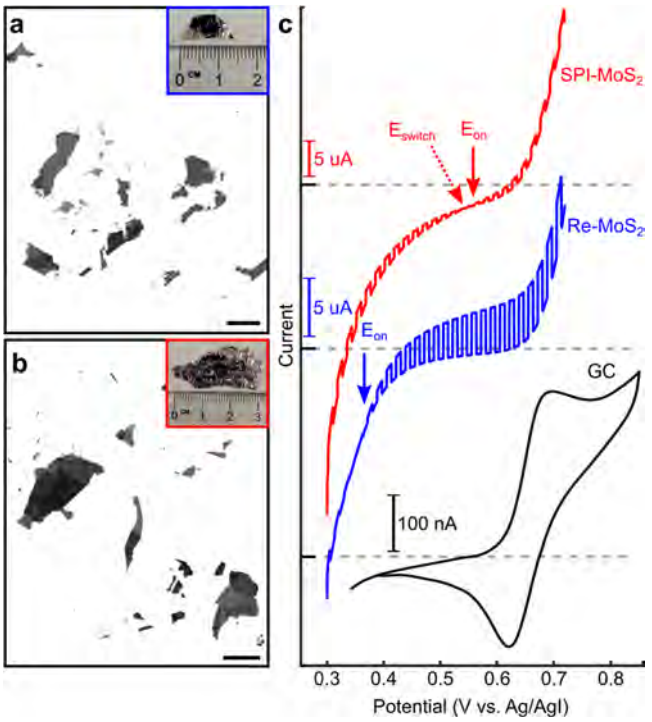

Figure 1. Optical and ensemble-level photoelectrochemical characterization of MoS_2 nanoflake photoelectrodes. Optical transmission images of (a) Re-MoS_2 and (b) SPI-MoS_2. Insets show photographs of the parent bulk crystals. Scale bars represent 100 μm. (c) LSV of Re-MoS_2 (blue) and SPI-MoS_2 (red) nanoflake films in aqueous 1 M NaI/1 mM I_2 electrolyte and under chopped light illumination (8 mW 532 nm LED illuminating a 2.5 cm^2 area). The black line represents a polished glassy carbon (GC) disk working electrode under dark conditions. The vertical red and blue arrows indicate the photocurrent onset potential (E_{on}).

approach, which allows us to quantitatively compare IQE values of individual Re-MoS_2 and SPI-MoS_2 nanoflakes that have different light absorption properties.

Figure 1c shows current–potential measurements of SPI-MoS_2 (top) and Re-MoS_2 (middle) in aqueous 1 M NaI/1 mM I_2 electrolyte under chopped light conditions. The anodic photocurrent for both samples increases with increasing positive potential, consistent with n-type semiconducting behavior.[1,25] The anodic photocurrent onset potential (E_{on}) of Re-MoS_2 and SPI-MoS_2 samples were 0.39 and 0.56 V vs Ag/AgI, respectively (indicated by vertical arrows in Figure 1c). These E_{on} values occur at more negative potentials than the iodide oxidation reaction on a polished GC disk electrode (Figure 1c, black trace). We also observed an anodic-to-cathodic photocurrent switching effect for SPI-MoS_2 (indicated by E_{switch} in Figure 1c, top). For potentials more negative than E_{switch}, SPI-MoS_2 exhibits an increasing cathodic photocurrent with increasing negative potential, consistent with p-type semiconducting behavior. This photocurrent switching has previously been shown for natural MoS_2 by Chen et al.[49] The photocurrent switching behavior suggests SPI-MoS_2 exhibits both p- and n-type photoelectrochemical properties. However, interpreting the ensemble-level observations in Figure 1c-top is challenging because the measurements do not reveal what fraction of SPI-MoS_2 nanoflakes are either n-type, p-type, or both. In this work, we use single nanoflake-level PEC measurements to address the sample heterogeneity

https://doi.org/10.1021/acsami.1c14928
ACS Appl. Mater. Interfaces XXXX, XXX, XXX–XXX

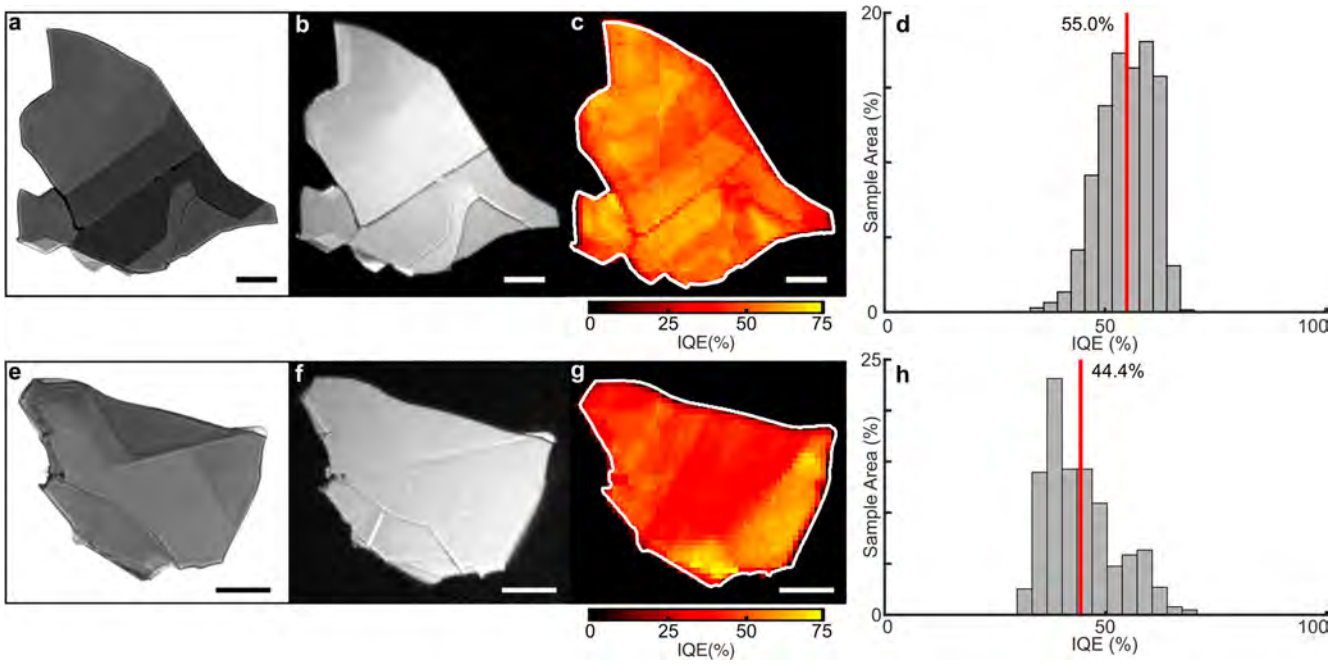

Figure 2. Single nanoflake photoelectrochemical measurements of Re-MoS_2. (a) Bright-field transmission image, (b) reflection image, and (c) IQE map of a 45 nm thick nanoflake. The IQE map was measured at +0.600 V vs Ag/AgI in aqueous 1 M NaI/1 mM I_2 electrolyte using a 860 nm-diameter 0.50 μW 415 nm laser. (d) Histogram of IQE values from the IQE map in c. (e–h) Same as in a–d, but for a 48 nm thick Re-MoS_2 nanoflake. All scale bars represent 10 μm.

issue and explore the origin of the n- and p-type photocurrent response in SPI-MoS_2.

In a typical single nanoflake PEC experiment, a 415 nm laser excites a 0.86 μm diameter spot on the nanoflake-coated ITO electrode, whereas a potentiostat measures the current of the entire electrochemical cell as a function of laser illumination position. We chose to map the photocurrent at fixed 0.600 V vs Ag/AgI because the photocurrent reaches a light-limited and potential-independent value at this potential, as evidenced by our previous ensemble-level studies[18] and local i–E measurements in Figure 4. IQE mapping with the 415 nm laser measures charge separation and collection efficiency of photogenerated electrons in the space charge region at the solid–liquid interface because the penetration depth (d) of the 415 nm light is 10 nm ($d = 1/\alpha(\lambda)$ and $\alpha(415\ \text{nm}) = 9 \times 10^5\ \text{cm}^{-1}$)[50] and we estimate from the Mott–Schottky equation that the space charge region thickness is 20 nm at an applied potential of 0.21 V versus the flatband potential ($E-E_{fb}$) and a doping density of $5 \times 10^{17}\ \text{cm}^{-3}$. Hence, the photocurrent dominantly stems from photons absorbed within the space charge region under these experimental conditions.

Figure 2a–d shows representative optical images and photocurrent mapping results from a single 45 nm thick Re-MoS_2 nanoflake under 415 nm excitation. The optical transmission images reveal differences in flake thickness (Figure 2a), whereas the reflection contrast reveals variations in surface step features (Figure 2b). Comparing the reflection and transmission images to the IQE map in Figure 2c reveals how nanoflake structural properties influence the photocurrent response: the photocurrent is uniform within a single basal plane and decreases when the laser spot moves across step edges. In addition, the dark red contrast at the nanoflake perimeter indicates lower anodic photocurrents at perimeter edge sites. Hence, illuminated edge sites produce lower anodic photocurrents, in agreement with previous spatially resolved measurements of bulk n-type WSe_2, WS_2, and $MoSe_2$ photoelectrodes that showed edge sites are recombination centers in iodide-based electrolytes.[38,51] Figure 2d shows the IQE distribution from the nanoflake in Figure 2a–c. The average IQE value is 55.0 ± 8.0% (S.D.), in agreement with IQE values for n-type WSe_2 single crystals reported by Kline and Parkinson.[1] We observed similarly high IQE values for other nanoflakes (Figure 2e–h). The average IQE from 21 nanoflakes studied herein was 38.2 ± 15.3% (Figure S3). Differences in charge separation efficiency or interfacial charge transfer kinetics could explain the IQE differences between Re-MoS_2 nanoflakes of similar thickness (see Figure 2). Spatial variations in bulk or surface defects can influence charge recombination in the space charge region or interfacial charge transfer rates.[52] Another possibility is the nanoflake surface area; larger nanoflakes generally have longer charge transport distances from the illumination spot to perimeter edge sites where electron–hole recombination can occur.[18]

Our group previously mapped 53 mechanically exfoliated $MoSe_2$ nanoflakes and observed 66% of nanoflakes were inactive "spectators",[18] meaning the flakes did not produce a photocurrent larger than the indium tin oxide (ITO) substrate. In that study, we hypothesized that poor electrical contact between $MoSe_2$ nanoflakes and ITO substrate was responsible for the large spectator population. The results in Figure 2 suggest that poor electrical contact cannot entirely account for the large population of inactive $MoSe_2$ nanoflakes because all active Re-MoS_2 nanoflakes in this work share the same contact with the ITO substrate in the $MoSe_2$ study. This work explores an alternative hypothesis to explain the origin of poor photocurrent collection efficiency in mechanically exfoliated nanoflakes: doping heterogeneity in the parent material limits PEC performance.

Photocurrent mapping experiments of SPI-MoS_2 nanoflakes revealed strikingly different photoelectrochemical behavior

https://doi.org/10.1021/acsami.1c14928
ACS Appl. Mater. Interfaces XXXX, XXX, XXX–XXX

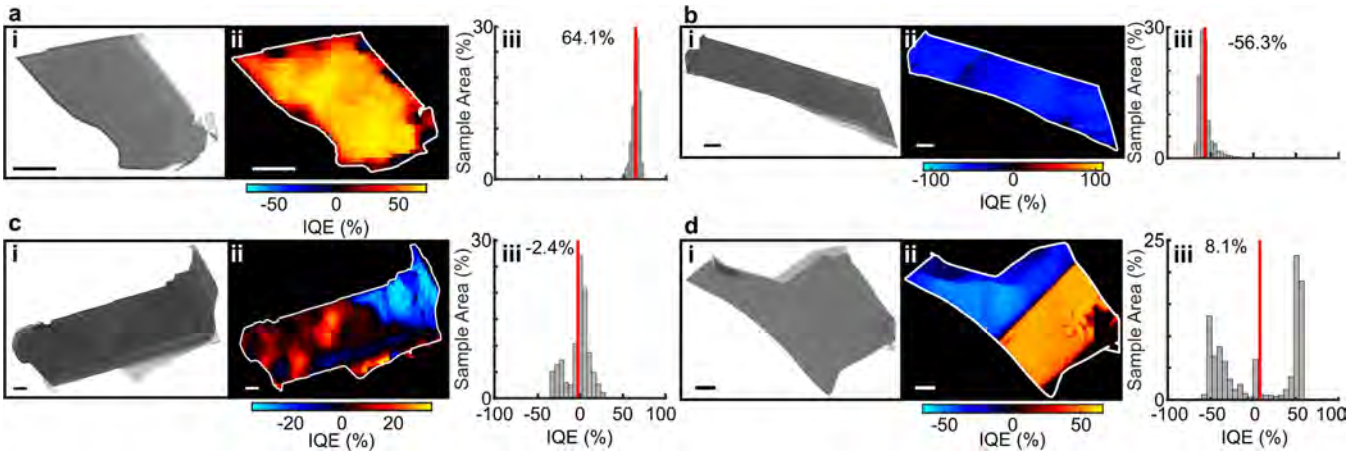

Figure 3. Single nanoflake photoelectrochemical measurements of SPI-MoS_2. Representative photocurrent maps of (a) 16 nm thick n-type nanoflake, (b) 63 nm thick p-type nanoflake, and (c, d) mixed n-type and p-type within a (c) 63 nm thick and (d) 70 nm thick nanoflake. Panels i–iii represent bright-field transmission images, IQE maps, and IQE distributions, respectively. IQE maps were measured at +0.600 V vs Ag/AgI in aqueous 1 M NaI/1 mM I_2 electrolyte using a 860 nm diameter, 0.50 μW 415 nm laser. All scale bars are 10 μm.

than the Re-MoS_2 nanoflakes. We classified SPI-MoS_2 nanoflake behaviors into three categories: (1) dominant n-type behavior, (2) dominant p-type behavior, and (3) mixed n- and p-type behavior. The categories were quantitatively based on the area fraction of a nanoflake that exhibited an n- or p-type photocurrent response. We defined dominant n-type behavior as >75% of the nanoflake area producing EQE values >1%. Figure 3a shows representative photocurrent mapping results of an n-type SPI-MoS_2 nanoflake. The nanoflake exhibits uniform n-type photoactivity across the main basal plane and low or no activity near the perimeter edges. Twelve out of 52 (23%) SPI-MoS_2 nanoflakes exhibited similar behavior (Figure S4 shows more examples). The inactive perimeter edges were striking in SPI-MoS_2 nanoflakes and were also present in our previous study of $MoSe_2$ nanoflakes. The inactive perimeter edges cannot be explained by the exfoliation process because the Re-MoS_2 nanoflakes did not show this effect and undergo the same exfoliation procedure. Instead, the inactive edges in SPI-MoS_2 and synthetic $MoSe_2$ are likely due to the doping heterogeneity effects discussed below.

On the other hand, 9 out of 52 (17%) SPI-MoS_2 nanoflakes exhibited dominant p-type behavior (Figure 3b and Figure S5). We defined dominant p-type nanoflakes as those flakes with >75% of the nanoflake area producing EQE < −1%. The negative EQE values indicate steady-state cathodic photocurrents due to the photoelectrochemical reduction of I_3^- and are represented as blue contrast in IQE maps. Interestingly, the mean cathodic IQE of p-type nanoflakes is nearly as efficient as the mean anodic IQE of n-type nanoflakes (Figure 3a-iii vs Figure 3b-iii). We observed no clear trend between IQE and layer thickness for either the n- or p-type domains (Figure S6). This trend indicates that photocurrent generation stems from carriers generated within the 20 nm thick space charge region. These results show the parent SPI-MoS_2 crystal contains both n- and p-type domains and the individual domains are nearly equally efficient under focused laser illumination (i.e., upon photoexcitation of a single domain).

Single nanoflake-level measurements also revealed intra-nanoflake doping heterogeneity in SPI-MoS_2. For 31 out of 52 nanoflakes, n- and p-type domains appeared within a single nanoflake (Figure 3c-i–iii and more examples in Figure S7). In 39% of nanoflakes, we observed large n- and p-type domains separated by sharp boundaries (Figure 3d,i–iii and more examples in Figure S8). The average fractional areas of the n- and p-type domains were 17 ± 27% and 37 ± 41%, respectively. Of all the nanoflakes with intrananoflake doping heterogeneity, 71% exhibited a mean anodic current response at fixed +0.6 V (Figure 3d-ii). The remaining 29% yielded a net cathodic photocurrent response (Figure 3c-iii). The fact that more nanoflakes exhibit n-type behavior agrees with the net anodic photocurrent magnitude at +0.6 V in ensemble-average photocurrent–voltage curves (Figure 1c, top). The average IQE value of SPI-MoS_2 nanoflakes is five times smaller than that of Re-MoS_2 (Figure S3b). Interestingly, the locations of the n- and p-type domains in Figure 3c, d did not necessarily correlate with structural features apparent in optical reflection images or transmission images, suggesting that materials chemistry properties influence the local doping heterogeneity instead of physical properties such as layer thickness or step edges. We note that optical transmission and reflection images cannot reveal fine structural details such as monolayer steps and variations in surface terminations at the boundary between n- and p-type domains. Another interesting feature of the mixed behavior nanoflakes is that the average value of the IQE distribution approaches 0% even though the IQE values from the individual n- and p-type regions exceed 10% (Figure 3c-iii). This low average value suggests that, upon illuminating the entire nanoflake, the sum of the photocurrents is nearly zero even though there are highly active n- and p-type domains within the nanoflake.

To further understand how the presence of n- and p-type domains in a single nanoflake contribute to the total nanoflake photocurrent, we measured i–E curves at single domains with a focused laser spot. The filled red circles in Figure 4a show i–E curves from three different n-type domains located on three different SPI-MoS_2 nanoflakes. Each curve displays n-type Schottky diode behavior: the photocurrent increases rapidly within 25 mV of E_{on} and increases steadily with increasingly positive potentials. Salvador and Pujadas previously observed a steep rise in initial photocurrent versus applied potential curves that mimic the lock-in detection conditions employed in this work.[53] The i–E curves from SPI-MoS_2 n-type domains varied more than those from Re-MoS_2 (filled blue circles in Figure

https://doi.org/10.1021/acsami.1c14928
ACS Appl. Mater. Interfaces XXXX, XXX, XXX–XXX

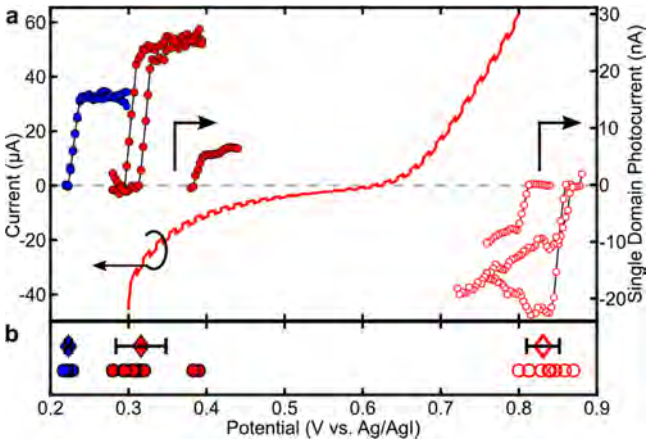

Figure 4. Single domain $i-E$ curves from Re-MoS_2 and SPI-MoS_2. (a) Ensemble-level chopped light LSV from Figure 1a (solid line, left axis). Single domain $i-E$ curves from 2 Re-MoS_2 nanoflakes (blue filled circles), 3 n-type SPI-MoS_2 domains (red filled circles), and 3 p-type SPI-MoS_2 domains (red open circles). The solid lines show ensemble-level $i-E$ curves from Figure 1a. (b) Distribution of E_{on} values from the individual domain curves in panel a (circles). The diamond markers indicate the average E_{on}. Error bars represent the standard deviation.

4a). As a result, the distribution of E_{on} values from natural SPI-MoS_2 nanoflakes was significantly larger than that on synthetic Re-MoS_2 nanoflakes (filled red versus filled blue circles in Figure 4b). Chaparro et al. also reported variations in E_{on} and $i-E$ curve shapes from different regions of bulk n-WSe_2 and n-$MoSe_2$ crystals.[43] Figure 4b quantitatively compares E_{on} values from SPI-MoS_2 and Re-MoS_2. The average E_{on} value of Re-MoS_2 was about 100 mV more negative than SPI-MoS_2 (0.223 ± 0.004 V versus 0.316 ± 0.032 V, see diamond symbols in Figure 4b). As E_{on} is equivalent to E_{fb} for ideal semiconductor/electrolyte interfaces (i.e., $E_{on} \approx E_{fb} = E_F - E^{0'}(I^-/I_2)$),[54] the more negative E_{on} value for Re-MoS_2 is likely due to a more negative Fermi level position on the electrochemical scale (E_F) as a result of higher doping density in the synthetic Re-doped crystals.

The $i-E$ curves from p-type domains display p-type Schottky diode behavior: the cathodic current rises sharply at E_{on} and increases steadily with increasingly negative potentials (open red circles in Figure 4a). The $i-E$ curves from the natural SPI-MoS_2 varied significantly from domain to domain, yielding a large distribution of E_{on} values (open red circles in Figure 4b). The differences between the individual i-E curves are likely due to spatial variations in doping density as well as bulk or surface defects that can influence charge recombination in the space charge region or interfacial charge transfer rates.[39,52] The average E_{on} value from the p-type domains was 0.831 ± 0.021 V. Importantly, none of the single domain $i-E$ curves from SPI-MoS_2 exhibited a photocurrent switching effect that was apparent in the ensemble-level measurement in Figure 1c. Therefore, the photocurrent switching effect observed at the ensemble-level in Figure 1c is likely caused by summing n- and p-type domain currents, which will be discussed below.

Materials Characterization. To understand the origin of doping heterogeneity in SPI-MoS_2, we analyzed the morphol-

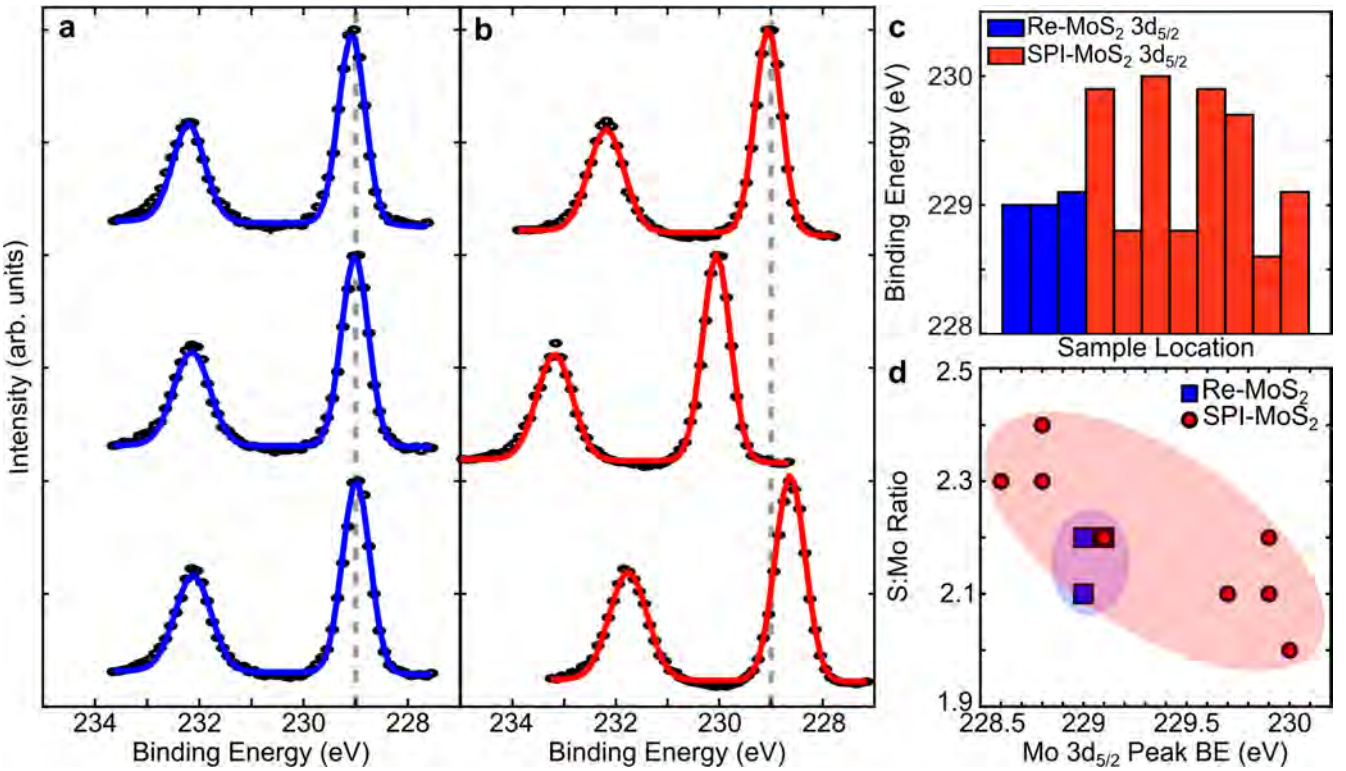

Figure 5. XPS analysis of Re-MoS_2 and SPI-MoS_2. (a, b) Spectra of the Mo 3d region from three separate locations on (a) Re-MoS_2 and (b) SPI-MoS_2. Solid blue and red lines represent fits to the data (solid circles). The vertical dashed gray lines represent the average Mo $3d_{5/2}$ peak position from all individual spectra. (c) Mo $3d_{5/2}$ peak positions for different sample locations. (d) S:Mo ratio, as determined from XPS peak fitting, versus the Mo $3d_{5/2}$ peak binding energy. The large red oval highlights the negative correlation between binding energy and S:Mo ratio for SPI-MoS_2. The small blue oval highlights the nearly constant binding energy and S:Mo ratio for Re-MoS_2.

https://doi.org/10.1021/acsami.1c14928
ACS Appl. Mater. Interfaces XXXX, XXX, XXX−XXX

ogy and composition of Re-MoS_2 and SPI-MoS_2 samples using ICP-AES, SEM-EDS, and XPS. Elemental analysis did not show significant composition variations between the samples (Table S1). If impurities are responsible for the p-type domains in SPI-MoS_2, then they are likely present in less than parts per billion concentrations, which is lower than the detection limit of the ICP-AES instrument. The flake morphologies appear qualitatively similar in SEM images (Figure S9) and no significant composition differences between the samples were observed in SEM-EDS, in agreement with the ICP-AES elemental analysis results.

XPS analysis revealed major differences between Re-MoS_2 and SPI-MoS_2. Figure 5a shows XPS spectra of the Mo 3d region measured from three different 800 μm^2 regions of freshly cleaved Re-MoS_2. The peak positions did not depend on sample position and the average binding energy from three locations was 229.0 ± 0.03 eV. On the other hand, the Mo 3d spectra from SPI-MoS_2 crystals vary from location to location (Figure 5b). Figure 5c compares the Mo $3d_{5/2}$ peak binding energy values from different regions of Re-MoS_2 and SPI-MoS_2 (see Figure S10 for S peak fitting results). The SPI-MoS_2 Mo $3d_{5/2}$ peak binding energy varies from 230.0 to 228.5 eV, whereas the Re-MoS_2 peak binding energy remains constant at 229.0 eV. For the SPI-MoS_2 sample, the peak shifts are accompanied by changes in the S:Mo atomic ratio (indicated by the large red oval in Figure 5d). The Mo $3d_{5/2}$ peak shifts to lower binding energy are correlated with higher S:Mo ratios. McDonnell et al. reported that this peak shift to lower binding energy can be explained by S-rich, p-type domains.[55,56] In this scenario, the peak shifts to lower binding energy because the Fermi level moves toward the valence band. The shifts in Mo binding energy are not attributed to a new chemical state as similar shifts in binding energy are observed for S 2p spectra. On the other hand, the Re-MoS_2 data localizes to a constant binding energy and S:Mo ratio (indicated by the small blue oval in Figure 5d).

DISCUSSION

Here we (1) discuss the likely origin and mechanism of doping heterogeneity in SPI-MoS_2 and (2) describe how the n- and p-type diode response of individual domains contributes to the total current of a single nanoflake.

Nonideal stoichiometry likely causes the doping heterogeneity in SPI-MoS_2. Our XPS data showed a sample location-dependent correlation between the S:Mo ratio and the Mo $3d_{5/2}$ peak binding energy (Figure 5). In 1968, Upadhyayula et al. linked the presence of excess chalcogen to p-type conductivity in synthetic WSe_2 crystals,[57] suggesting that the S-rich locations of the SPI-MoS_2 crystal studied herein are responsible for p-type photoelectrochemical behavior. Recent scanning tunneling spectroscopy (STS) and XPS measurements of SPI-MoS_2 crystals showed similar trends: S-rich regions of MoS_2 exhibit p-type behavior.[55] In addition, the Mo 3d and S 2p binding energies shifted to lower binding energy in S-rich regions, in agreement with our data in Figure 5. In 1981, Menezes and Lewerenz first demonstrated how the doping heterogeneity effect influenced photoelectrochemical performance in a I^-/I_3^- electrolyte similar to the one employed in this work.[40] The authors showed n- and p-type domains coexist in synthetic WSe_2 photoelectrodes grown by chemical vapor transport. The 0.06 mm^2 633 nm laser spot in those experiments was 10^5 times larger than the light spot employed herein, which prevented direct observation and quantification of domain sizes. Regardless, Menezes et al. attributed the doping heterogeneity to variations in Se concentration or segregation of impurities. The doping heterogeneity effect was also reported for other TMD materials and growth methods.[58]

Multiple mechanisms can explain the doping heterogeneity effect in bulk TMDs. Santosh et al. attributed n-type doping properties of MoS_2 to S vacancies.[59] The S vacancies produce defect states within the band gap, 0.6 eV below the conduction band minimum (CBM). These defect donor levels can contribute to the n-type character of S-deficient domains. However, other reports have disputed this mechanism.[60−64] Zhang et al. showed that S vacancies led to the formation of acceptor states just above the valence band maximum (VBM) and an upward shift of the VBM by 0.2 eV toward the Fermi level, consistent with p-type doping.[65] The STS study of the same SPI-MoS_2 crystals employed herein provide strong evidence that S-rich regions exhibit p-type doping behavior, suggesting the former mechanism can explain doping heterogeneity in these naturally occurring crystals. An alternative hypothesis is that a surface defect layer induces an inverted charge separation effect, as has been reported in Cu_2O nanoparticle photocatalysts.[66] However, we did not observe a thickness-dependent doping heterogeneity effect (Figure S6) that would likely be consistent with that mechanism. Regardless of the exact mechanism responsible for doping heterogeneity in these natural crystals, our spatially resolved $i-E$ measurements revealed the presence of n- and p-type domains within single exfoliated MoS_2 nanoflakes and quantified the distribution of domain sizes.

Differences in materials chemistry properties between the samples are the likely origin of the performance gap, rather than the sample preparation procedure. Both samples were mechanically exfoliated with low residue Nitto tape, consistent with literature.[46] The exfoliated Re-MoS_2 nanoflakes are highly active for photoelectrochemical iodide oxidation, as evidenced by IQE values on par with single-crystal MoS_2 photoelectrodes.[67] Hence, we conclude that the exfoliation procedure produces high-quality TMD nanoflakes and is likely not responsible for the differences between Re-MoS_2 and SPI-MoS_2.

Finally, we discuss how the photoelectrochemical properties of individual domains contribute to the total current under whole-flake illumination. If we illuminate an entire nanoflake, then the total nanoflake current will be the sum of the individual n- and p-type diode currents. The single domain $i-E$ measurements in Figure 4 show that the diode characteristics vary from domain to domain (i.e., onset potentials, ideality factors, and photocurrent saturation values). In the ensemble-level measurement, the large light spot illuminates an unknown number of domains with distinct diode characteristics. Scheme 1 schematically shows the summation current (solid black line) for two domains with different n- and p-type diode characteristics (dashed orange and blue lines, respectively). The summation current is an s-shaped curve that qualitatively agrees with the ensemble-average photoelectrochemical behavior, including the photocurrent switching effect, in Figure 1c (red line in Scheme 1). E_{switch} occurs about halfway between the E_{on} values of the n- and p-type domains.

This photocurrent averaging effect (i.e., summing n- and p-type diode current from neighboring n- and p-type domains) can also explain performance variation among apparently smooth basal planes. When the domain sizes become smaller

https://doi.org/10.1021/acsami.1c14928
ACS Appl. Mater. Interfaces XXXX, XXX, XXX−XXX

Scheme 1. Schematic Explanation of How Individual n- and p-type Domain Currents with Different Ideality Factors and Onset Potentials Contribute to the Ensemble-Level Photoelectrochemical Behavior[a]

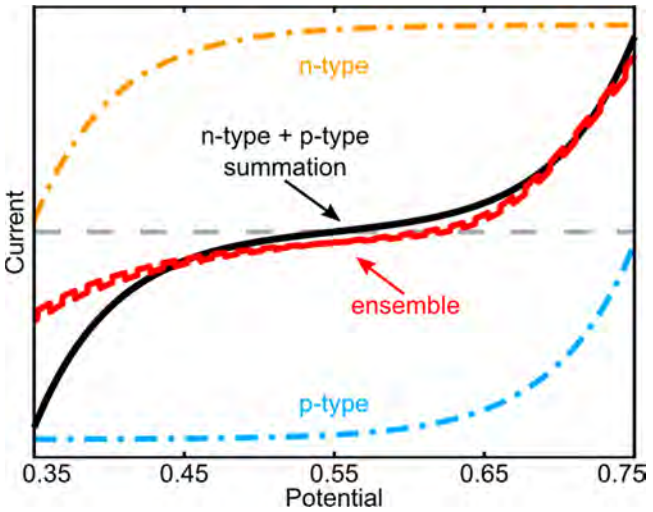

[a]The dot-dashed lines represent n- and p-type diode curves from individual domains, under constant illumination. The black line represents the sum of the individual curves. The red line is the ensemble-level experimental data for SPI-MoS_2 under chopped illumination, from Figure 1c.

than the laser spot size in our photocurrent mapping experiments, the photocurrent averaging effect occurs even though the illumination spot is very small. In this case, the small photocurrent will be assigned to the pixel in the photocurrent map, contributing to performance variation within apparently smooth basal places (see Figure 3c-ii).

CONCLUSION

TMD nanoflake electrodes exhibit lower PEC performance than bulk TMDs. Single nanoflake-level IQE mapping revealed n- and p-type domains within single nanoflakes. Average IQE values from single domains exceeded 60%, indicating that the individual n- and p-type domains were efficient for iodide oxidation and tri-iodide reduction, respectively. Single domain *i*−*E* curves showed diode-like responses that do not appear in the ensemble-level photoelectrochemical measurement. We propose that the sum of the n- and p-type diode currents cause the low ensemble-average PEC current response. XPS measurements indicate that the origin of the n- and p-type domains is likely nonideal stoichiometry within the parent crystal. Our findings contribute to the understanding of the origin of the performance gap between bulk and nanoflake TMD photoelectrodes. Furthermore, our work suggests that it may be possible to synthesize nanoflakes with lateral p−n junctions to enhance charge separation in TMD photocatalysts.

ASSOCIATED CONTENT

Supporting Information

The Supporting Information is available free of charge at https://pubs.acs.org/doi/10.1021/acsami.1c14928.

Laser line knife-edge scan, additional nanoflake images and IQE maps, SEM micrographs, additional XPS peak fitting results, elemental analysis results, description of data processing procedure for IQE and thickness calculations (PDF)

AUTHOR INFORMATION

Corresponding Author

Justin B. Sambur − *Department of Chemistry, Colorado State University, Fort Collins, Colorado 80523-1872, United States;* orcid.org/0000-0002-8457-4946; Email: jsambur@colostate.edu

Author

Michael Van Erdewyk − *Department of Chemistry, Colorado State University, Fort Collins, Colorado 80523-1872, United States;* orcid.org/0000-0002-9502-7155

Complete contact information is available at: https://pubs.acs.org/10.1021/acsami.1c14928

Author Contributions

M.V.E performed experiments and analyzed data. M.V.E. and J.B.S. designed experiments and wrote the manuscript.

Funding

This research was supported by the U.S. Department of Energy, Office of Science, Office of Basic Energy Sciences, under Award DE-SC0021189.

Notes

The authors declare no competing financial interest.

ACKNOWLEDGMENTS

The authors thank Dr. Rebecca Miller and the CSU-ARC for XPS and SEM-EDS measurements. The authors thank Prof. Jamie Neilson for the Horiba monochromatic illumination source. ICP-AES measurements were performed by the Colorado State University Soil Testing Lab.

ABBREVIATIONS

XPS, X-ray photoelectron spectroscopy; ITO, tin doped indium oxide; PEC, photoelectrochemical; TMD, transition metal dichalcogenide; EQE, external quantum efficiency; IQE, internal quantum efficiency; *i*−*E*, photocurrent−potential; 2D, two-dimensional; GC, glassy carbon; ICP-AES, inductively coupled plasma atomic emission spectroscopy; SEM, scanning electron microscopy; EDS, energy-dispersive X-ray spectroscopy; DAQ, data acquisition

REFERENCES

(1) Kline, G.; Kam, K.; Canfield, D.; Parkinson, B. A. Efficient and Stable Photoelectrochemical Cells Constructed with WSe_2 and $MoSe_2$ Photoanodes. *Sol. Energy Mater.* **1981**, *4* (3), 301−308.

(2) Tributsch, H. Solar Energy-Assisted Electrochemical Splitting of Water. Some Energetical, Kinetical and Catalytical Considerations Verified on MoS_2 Layer Crystal Surfaces. *Z. Naturforsch., A: Phys. Sci.* **1977**, *32* (9), 972−985.

(3) Gobrecht, J.; Tributsch, H.; Gerischer, H. Performance of Synthetical n-$MoSe_2$ in Electrochemical Solar Cells. *J. Electrochem. Soc.* **1978**, *125* (12), 2085.

(4) Lewerenz, H. J.; Heller, A.; DiSalvo, F. J. Relationship between Surface Morphology and Solar Conversion Efficiency of Tungsten Diselenide Photoanodes. *J. Am. Chem. Soc.* **1980**, *102* (6), 1877−1880.

(5) Tenne, R.; Wold, A. Passivation of Recombination Centers in n-WSe_2 Yields High Efficiency (>14%) Photoelectrochemical Cell. *Appl. Phys. Lett.* **1985**, *47* (7), 707−709.

(6) Yu, X.; Sivula, K. Toward Large-Area Solar Energy Conversion with Semiconducting 2D Transition Metal Dichalcogenides. *ACS Energy Lett.* **2016**, *1* (1), 315−322.
(7) Li, C.; Cao, Q.; Wang, F.; Xiao, Y.; Li, Y.; Delaunay, J.-J.; Zhu, H. Engineering Graphene and TMDs Based van Der Waals Heterostructures for Photovoltaic and Photoelectrochemical Solar Energy Conversion. *Chem. Soc. Rev.* **2018**, *47* (13), 4981−5037.
(8) Ganguly, P.; Harb, M.; Cao, Z.; Cavallo, L.; Breen, A.; Dervin, S.; Dionysiou, D. D.; Pillai, S. C. 2D Nanomaterials for Photocatalytic Hydrogen Production. *ACS Energy Lett.* **2019**, *4* (7), 1687−1709.
(9) Wells, R. A.; Johnson, H.; Lhermitte, C. R.; Kinge, S.; Sivula, K. Roll-to-Roll Deposition of Semiconducting 2D Nanoflake Films of Transition Metal Dichalcogenides for Optoelectronic Applications. *ACS Appl. Nano Mater.* **2019**, *2* (12), 7705−7712.
(10) Magda, G. Z.; Petö, J.; Dobrik, G.; Hwang, C.; Biró, L. P.; Tapasztó, L. Exfoliation of Large-Area Transition Metal Chalcogenide Single Layers. *Sci. Rep.* **2015**, *5* (1), 14714.
(11) Liu, F.; Wu, W.; Bai, Y.; Chae, S. H.; Li, Q.; Wang, J.; Hone, J.; Zhu, X.-Y. Disassembling 2D van Der Waals Crystals into Macroscopic Monolayers and Reassembling into Artificial Lattices. *Science* **2020**, *367* (6480), 903−906.
(12) Duong, D. L.; Yun, S. J.; Lee, Y. H. Van Der Waals Layered Materials: Opportunities and Challenges. *ACS Nano* **2017**, *11* (12), 11803−11830.
(13) Song, X.; Guo, Z.; Zhang, Q.; Zhou, P.; Bao, W.; Zhang, D. W. Progress of Large-Scale Synthesis and Electronic Device Application of Two-Dimensional Transition Metal Dichalcogenides. *Small* **2017**, *13* (35), 1700098.
(14) Wang, P.; Yang, D.; Pi, X. Toward Wafer-Scale Production of 2D Transition Metal Chalcogenides. *Adv. Electron. Mater.* **2021**, *7* (8), 2100278.
(15) Tributsch, H. Electrochemical Solar Cells Based on Layer-Type Transition Metal Compounds: Performance of Electrode Material. *Sol. Energy Mater.* **1979**, *1* (3), 257−269.
(16) Fan, F.-R. F.; White, H. S.; Wheeler, B.; Bard, A. J. Semiconductor Electrodes: XXIX. High Efficiency Photoelectrochemical Solar Cells with Electrodes in an Aqueous Iodide Medium. *J. Electrochem. Soc.* **1980**, *127* (2), 518.
(17) Kline, G.; Kam, K. K.; Ziegler, R.; Parkinson, B. A. Further Studies of the Photoelectrochemical Properties of the Group VI Transition Metal Dichalcogenides. *Sol. Energy Mater.* **1982**, *6* (3), 337−350.
(18) Todt, M. A.; Isenberg, A. E.; Nanayakkara, S. U.; Miller, E. M.; Sambur, J. B. Single-Nanoflake Photo-Electrochemistry Reveals Champion and Spectator Flakes in Exfoliated $MoSe_2$ Films. *J. Phys. Chem. C* **2018**, *122* (12), 6539−6545.
(19) Isenberg, A. E.; Todt, M. A.; Wang, L.; Sambur, J. B. The Role of Photogenerated Iodine on the Energy Conversion Properties of $MoSe_2$ Nanoflake Liquid Junction Photovoltaics. *ACS Appl. Mater. Interfaces* **2018**, *10*, 27780.
(20) McKone, J. R.; Pieterick, A. P.; Gray, H. B.; Lewis, N. S. Hydrogen Evolution from Pt/Ru-Coated p-Type WSe_2 Photocathodes. *J. Am. Chem. Soc.* **2013**, *135* (1), 223−231.
(21) Yu, X.; Prévot, M. S.; Guijarro, N.; Sivula, K. Self-Assembled 2D WSe_2 Thin Films for Photoelectrochemical Hydrogen Production. *Nat. Commun.* **2015**, *6* (1), 7596.
(22) Yu, X.; Guijarro, N.; Johnson, M.; Sivula, K. Defect Mitigation of Solution-Processed 2D WSe_2 Nanoflakes for Solar-to-Hydrogen Conversion. *Nano Lett.* **2018**, *18* (1), 215−222.
(23) Gobrecht, J.; Gerischer, H.; Tributsch, H. Electrochemical Solar Cell Based on the D-Band Semiconductor Tungsten-Diselenide. *Ber. Bunsen. Phys. Chem.* **1978**, *82* (12), 1331−1335.
(24) Parkinson, B. A.; Furtak, T. E.; Canfield, D.; Kam, K.-K.; Kline, G. Evaluation and Reduction of Efficiency Losses at Tungsten Diselenide Photoanodes. *Faraday Discuss. Chem. Soc.* **1980**, *70* (0), 233−245.
(25) Fan, F.-R. F.; Bard, A. J. Semiconductor Electrodes: XXXVI. Characteristics of, Electrodes in Aqueous Solution. *J. Electrochem. Soc.* **1981**, *128* (5), 945.
(26) Lewerenz, H. J.; Gerischer, H.; Lübke, M. Photoelectrochemistry of WSe_2 Electrodes: Comparison of Stepped and Smooth Surfaces. *J. Electrochem. Soc.* **1984**, *131* (1), 100.
(27) Kautek, W.; Gerischer, H.; Tributsch, H. The Role of Surface Orientation in the Photoelectrochemical Behavior of Layer Type D-Band Semiconductors. *Ber. Bunsen. Phys. Chem.* **1979**, *83* (10), 1000−1008.
(28) Salvador, P.; Chaparro, A. M.; Mir, A. Digital Imaging of the Effect of Photoetching on the Photoresponse of n-Type Tungsten Diselenide and Molybdenum Diselenide Single Crystal Electrodes. *J. Phys. Chem.* **1996**, *100* (2), 760−768.
(29) Velazquez, J. M.; John, J.; Esposito, D. V.; Pieterick, A.; Pala, R.; Sun, G.; Zhou, X.; Huang, Z.; Ardo, S.; Soriaga, M. P.; et al. A Scanning Probe Investigation of the Role of Surface Motifs in the Behavior of p-WSe_2 Photocathodes. *Energy Environ. Sci.* **2016**, *9* (1), 164−175.
(30) Eisenberg, D. Imaging the Anisotropic Reactivity of a Tungsten Diselenide Photocathode. *ChemElectroChem* **2015**, *2* (9), 1259−1263.
(31) Canfield, D.; Parkinson, B. A. Improvement of Energy Conversion Efficiency by Specific Chemical Treatments of Molybdenum Selenide (n-$MoSe_2$) and Tungsten Selenide (n-WSe_2) Photoanodes. *J. Am. Chem. Soc.* **1981**, *103* (5), 1279−1281.
(32) White, H. S.; Abruna, H. D.; Bard, A. J. Semiconductor Electrodes: XLI. Improvement of Performance of Electrodes by Electrochemical Polymerization of O-Phenylenediamine at Surface Imperfections. *J. Electrochem. Soc.* **1982**, *129* (2), 265.
(33) Shearer, M. J.; Li, W.; Foster, J. G.; Stolt, M. J.; Hamers, R. J.; Jin, S. Removing Defects in WSe_2 via Surface Oxidation and Etching to Improve Solar Conversion Performance. *ACS Energy Lett.* **2019**, *4* (1), 102−109.
(34) Velický, M.; Bissett, M. A.; Woods, C. R.; Toth, P. S.; Georgiou, T.; Kinloch, I. A.; Novoselov, K. S.; Dryfe, R. A. W. Photoelectrochemistry of Pristine Mono- and Few-Layer MoS_2. *Nano Lett.* **2016**, *16* (3), 2023−2032.
(35) Hill, J. W.; Hill, C. M. Directly Mapping Photoelectrochemical Behavior within Individual Transition Metal Dichalcogenide Nanosheets. *Nano Lett.* **2019**, *19* (8), 5710−5716.
(36) Takahashi, Y.; Kobayashi, Y.; Wang, Z.; Ito, Y.; Ota, M.; Ida, H.; Kumatani, A.; Miyazawa, K.; Fujita, T.; Shiku, H.; Korchev, Y. E.; Miyata, Y.; Fukuma, T.; Chen, M.; Matsue, T. High-Resolution Electrochemical Mapping of the Hydrogen Evolution Reaction on Transition-Metal Dichalcogenide Nanosheets. *Angew. Chem., Int. Ed.* **2020**, *59* (9), 3601−3608.
(37) Hill, J. W.; Fu, Z.; Tian, J.; Hill, C. M. Locally Engineering and Interrogating the Photoelectrochemical Behavior of Defects in Transition Metal Dichalcogenides. *J. Phys. Chem. C* **2020**, *124* (31), 17141−17149.
(38) Tóth, P. S.; Szabó, G.; Janáky, C. Structural Features Dictate the Photoelectrochemical Activities of Two-Dimensional $MoSe_2$ and WSe_2 Nanostructures. *J. Phys. Chem. C* **2021**, *125* (14), 7701−7710.
(39) Tolbert, C. L.; Hill, C. Electrochemically Probing Exciton Transport in Monolayers of Two-Dimensional Semiconductors *Faraday Discuss.* **2021**, DOI: 10.1039/D1FD00052G.
(40) Menezes, S.; Schneemeyer, L. F.; Lewerenz, H. J. Efficiency Losses from Carrier-type Inhomogeneity in Tungsten Diselenide Photoelectrodes. *Appl. Phys. Lett.* **1981**, *38* (11), 949−951.
(41) Bicelli, L. P.; Razzini, G. Surface Defects on n-$MoSe_2$ Electrodes Used in Photoelectrochemical Solar Cells. *Surf. Technol.* **1983**, *20* (4), 383−392.
(42) Furtak, T. E.; Canfield, D. C.; Parkinson, B. A. Scanning Light-spot Analysis of the Carrier Collection in Liquid-junction Solar Energy Converters. *J. Appl. Phys.* **1980**, *51* (11), 6018−6021.
(43) Chaparro, A. M.; Salvador, P.; Mir, A. The Scanning Microscope for Semiconductor Characterization: Photocurrent, Photovoltage and Electrolyte Electroreflectance Imaging at the n-$MoSe_2/I^-$ Interface. *J. Electroanal. Chem.* **1997**, *424* (1), 153−157.
(44) Zhang, Y.; Ye, J.; Matsuhashi, Y.; Iwasa, Y. Ambipolar MoS_2 Thin Flake Transistors. *Nano Lett.* **2012**, *12* (3), 1136−1140.

https://doi.org/10.1021/acsami.1c14928
ACS Appl. Mater. Interfaces XXXX, XXX, XXX−XXX

(45) Fang, N.; Toyoda, S.; Taniguchi, T.; Watanabe, K.; Nagashio, K. Full Energy Spectra of Interface State Densities for n- and p-Type MoS_2 Field-Effect Transistors. *Adv. Funct. Mater.* **2019**, *29* (49), 1904465.
(46) Castellanos-Gomez, A.; Buscema, M.; Molenaar, R.; Singh, V.; Janssen, L.; van der Zant, H. S J; Steele, G. A Deterministic Transfer of Two-Dimensional Materials by All-Dry Viscoelastic Stamping. *2D Mater.* **2014**, *1* (1), 011002.
(47) Wang, L.; Sambur, J. B. Efficient Ultrathin Liquid Junction Photovoltaics Based on Transition Metal Dichalcogenides. *Nano Lett.* **2019**, *19* (5), 2960−2967.
(48) Sales, M. G.; Herweyer, L.; Opila, E.; McDonnell, S. MoS_2 Impurities: Chemical Identification and Spatial Resolution of Bismuth Impurities in Geological Material. *Appl. Surf. Sci.* **2020**, *508*, 145256.
(49) Chen, Z.; Forman, A. J.; Jaramillo, T. F. Bridging the Gap Between Bulk and Nanostructured Photoelectrodes: The Impact of Surface States on the Electrocatalytic and Photoelectrochemical Properties of MoS_2. *J. Phys. Chem. C* **2013**, *117* (19), 9713−9722.
(50) Frindt, R. F.; Yoffe, A. D.; Bowden, F. P. Physical Properties of Layer Structures: Optical Properties and Photoconductivity of Thin Crystals of Molybdenum Disulphide. *Proc. R. Soc. A* **1963**, *273* (1352), 69−83.
(51) Hill, J. W.; Hill, C. Directly Visualizing Carrier Transport and Recombination at Individual Defects within 2D Semiconductors. *Chem. Sci.* **2021**, *12*, 5102.
(52) Reichman, J. The Current-voltage Characteristics of Semiconductor-electrolyte Junction Photovoltaic Cells. *Appl. Phys. Lett.* **1980**, *36* (7), 574−577.
(53) Salvador, P.; Pujadas, M.; Campet, G. Photoreactions at the n-Type-WSe_2−Electrolyte Interface: Study by Electrolyte Electroreflectance and Photocurrent Transient Measurements. *Phys. Rev. B: Condens. Matter Mater. Phys.* **1988**, *38* (14), 9881−9888.
(54) Cooper, G.; Turner, J. A.; Nozik, A. J. Mott-Schottky Plots and Flatband Potentials for Single Crystal Rutile Electrodes. *J. Electrochem. Soc.* **1982**, *129* (9), 1973.
(55) McDonnell, S.; Addou, R.; Buie, C.; Wallace, R. M.; Hinkle, C. L. Defect-Dominated Doping and Contact Resistance in MoS_2. *ACS Nano* **2014**, *8* (3), 2880−2888.
(56) Addou, R.; McDonnell, S.; Barrera, D.; Guo, Z.; Azcatl, A.; Wang, J.; Zhu, H.; Hinkle, C. L.; Quevedo-Lopez, M.; Alshareef, H. N.; Colombo, L.; Hsu, J. W. P.; Wallace, R. M. Impurities and Electronic Property Variations of Natural MoS_2 Crystal Surfaces. *ACS Nano* **2015**, *9* (9), 9124−9133.
(57) Upadhyayula, L. C.; Loferski, J. J.; Wold, A.; Giriat, W.; Kershaw, R. Semiconducting Properties of Single Crystals of n- and p-Type Tungsten Diselenide (WSe_2). *J. Appl. Phys.* **1968**, *39* (10), 4736−4740.
(58) Hofmann, W. K.; Lewerenz, H. J. Improved Photoactivity of Melt-Grown Group VI Transition Metal Dichalcogenides: Preparation from Se and Se-Te Melts. *Sol. Energy Mater.* **1988**, *17* (5), 369−374.
(59) KC, S.; Longo, R. C.; Addou, R.; Wallace, R. M.; Cho, K. Impact of Intrinsic Atomic Defects on the Electronic Structure of MoS_2 monolayers. *Nanotechnology* **2014**, *25* (37), 375703.
(60) Brandão, F. D.; Ribeiro, G. M.; Vaz, P. H.; González, J. C.; Krambrock, K. Identification of Rhenium Donors and Sulfur Vacancy Acceptors in Layered MoS_2 Bulk Samples. *J. Appl. Phys.* **2016**, *119* (23), 235701.
(61) Komsa, H.-P.; Krasheninnikov, A. V. Native Defects in Bulk and Monolayer MoS_2 from First Principles. *Phys. Rev. B: Condens. Matter Mater. Phys.* **2015**, *91* (12), 125304.
(62) Noh, J.-Y.; Kim, H.; Kim, Y.-S. Stability and Electronic Structures of Native Defects in Single-Layer MoS_2. *Phys. Rev. B: Condens. Matter Mater. Phys.* **2014**, *89* (20), 205417.
(63) Singh, A.; Singh, A. K. Origin of n-Type Conductivity of Monolayer MoS_2. *Phys. Rev. B: Condens. Matter Mater. Phys.* **2019**, *99* (12), 121201.
(64) Rao, R.; Carozo, V.; Wang, Y.; Islam, A. E.; Perea-Lopez, N.; Fujisawa, K.; Crespi, V. H.; Terrones, M.; Maruyama, B. Dynamics of Cleaning, Passivating and Doping Monolayer MoS_2 by Controlled Laser Irradiation. *2D Mater.* **2019**, *6* (4), 045031.
(65) Zhang, X.; Wang, S.; Lee, C.-K.; Cheng, C.-M.; Lan, J.-C.; Li, X.; Qiao, J.; Tao, X. Unravelling the Effect of Sulfur Vacancies on the Electronic Structure of the MoS_2 Crystal. *Phys. Chem. Chem. Phys.* **2020**, *22* (38), 21776−21783.
(66) Chen, R.; Pang, S.; An, H.; Dittrich, T.; Fan, F.; Li, C. Giant Defect-Induced Effects on Nanoscale Charge Separation in Semiconductor Photocatalysts. *Nano Lett.* **2019**, *19* (1), 426−432.
(67) Kam, K. K.; Parkinson, B. A. Detailed Photocurrent Spectroscopy of the Semiconducting Group VIB Transition Metal Dichalcogenides. *J. Phys. Chem.* **1982**, *86* (4), 463−467.

https://doi.org/10.1021/acsami.1c14928
ACS Appl. Mater. Interfaces XXXX, XXX, XXX−XXX